Dynamics of strong-field above-threshold ionization of argon: Comparison between experiment and theory

Rolf Wiehle, Bernd Witzel, and Hanspeter Helm

Fakultät für Physik, Albert-Ludwigs-Universität, Stefan-Meier-Strasse 19, D-79104 Freiburg, Germany

Eric Cormier*

*Centre Lasers Intenses et Applications, UMR 5107 du CNRS, Université Bordeaux I, 351 Cours de la Libération,
F-33405 Talence, France*

We record angle-resolved electron-momentum distributions from 800-nm short-pulse laser ionization of argon and compare our data with numerical solutions of the time-dependent Schrödinger equation. A model potential of argon and the single active electron approximation are used. The calculation shows quantitative agreement in all dominant features of the experimental results. The energy and angular distributions of the photoelectrons, together with numerical simulations, allow us to identify the multiple processes involved during the interaction, such as channel switching, multiphoton resonant and nonresonant ionization, and ac Stark splitting.

I. INTRODUCTION

Electron energy distributions from multiphoton ionization processes have been an active topic of research since laser systems are able to deliver short pulses. Experimental as well as theoretical works of the last years mainly concentrate their efforts on the high-energy part of the photoelectron spectrum dominated by an electron distribution due to above-threshold ionization (ATI) processes. Typical features such as plateau and jet structures in the energy spectrum can be observed [1] and interpreted [2]. Only little work has been reported on the intensity dependence of the momentum resolved photoelectron spectrum at low kinetic electron energy [3], and a detailed comparison of current state-of-the-art theory and experiment is missing. Particularly, the presence of highly resolved structures (Freeman resonances [4]) in the electron momentum distributions leads to a detailed analysis of transient resonances, playing a crucial role in the understanding of short-pulse laser ionization dynamics [5]. Here we give an account of a joint experimental-theoretical effort to analyze the complex angular and energy patterns that appear in strong-field ionization of argon. The very significant dependence of the photoelectron energy and angular distributions on the peak laser intensity is shown to be quantitatively accounted for in the single active electron approximation.

II. EXPERIMENT

A. Experimental setup

A linearly polarized Ti:sapphire laser beam ($\tau = 100$ fs, $E_{max} = 1$ mJ) is focussed into a vacuum chamber containing argon gas at pressures varying between 10^{-7} and 10^{-4} mbar. The wavelength is centered at 800 nm with a full width at half maximum (FWHM) of 9 nm. The pulse duration is

monitored continuously with an interferometric autocorrelator and the maximum laser intensity can be varied by a half-wave plate and a polarizing beam splitter. A photoelectron imaging spectrometer [6] is used to record momentum resolved photoelectron distribution of the ionization process. A constant electric field of 100 V/cm allows the projection of the photoelectrons onto a two-dimensional detector consisting of a pair of multichannel plates and a phosphor screen. Electron impact positions are recorded with a computer based charge-coupled device (CCD) camera. The software, in combination with the high repetition rate of the laser of 1 kHz, allows the accumulation of $10^5 - 10^7$ single-electron signals per image. Electrons created with the same kinetic energy appear inside a well defined circular pattern. The radius is proportional to the momentum of the electron. Each image contains the signal of photoelectrons created by different processes, resulting in a superposition of many corresponding patterns. Because the photoelectron distribution is symmetric with respect to the polarization axis of the linearly polarized laser, an inverse Abelian transformation can be used to convert the images into angle-resolved momentum distributions [7]. The center of the transformed images corresponds to zero momentum. The distance from the center to a particular point is proportional to the electrons' momentum.

B. Laser peak intensity calibration

From the measured pulse energy of the laser we determine the peak intensity in two independent ways. Since the electronic energies vary with intensity (Stark effect), excited states successively shift into resonance with multiphoton absorption when the intensity is increased. Excited atoms ionized with one photon produce photoelectrons with the characteristic signature of the excited state. The appearance of a peak in the electron spectrum at a given pulse energy corresponds to the laser intensity required to shift a Rydberg state into resonance. The calibration (relation between laser inten-

―――――
*Electronic address: Eric.Cormier@celia.u-bordeaux.fr
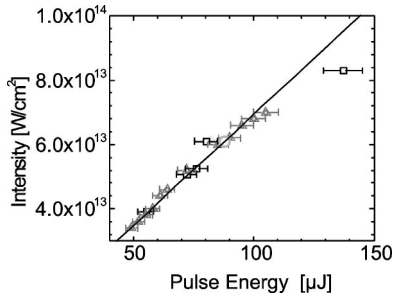
FIG. 1. Intensity calibration as a function of the recorded pulse energy. Open squares, resonance opening. Open triangles, direct comparison with theory. Open circle, channel switching. Full line, linear fit.

sity and pulse energy) is realized by assigning a Rydberg resonance to the pulse energy for which the peak appears (see Fig. 1), assuming ponderomotive shifting of the excited state energy. This coarse intensity calibration is refined with the following procedure. The remarkable agreement between the measured photoelectron spectra [see, e.g., Figs. 2(a) to 2(f)] and the ones predicted by theory offers the opportunity to assign an intensity to various experimentally gained spectra by comparing them with theory.

The intensity calibration is reenforced by comparing the contrast $m(E)$ of the experimental photoelectron energy spectra with the calculated ones:

$$m(E) = \frac{f_{max}(E) - f_{min}(E)}{f_{max}(E) + f_{min}(E)}, \quad (1)$$

where $f_{max}(E) = \max(f(E'))$ for $E' \in [E - \frac{1}{2}\hbar\omega, E + \frac{1}{2}\hbar\omega]$ and $f(E)$ is the number of electrons collected with a kinetic energy of E. $f_{min}(E)$ is defined in a similar manner. The contrast for any given energy taken as a function of the laser intensity exhibits a distinct minimum between two channel closures [8]. The contrast minimum intensity observed in the experiment and the calculation can be taken as a further means to judge our intensity calibration. As a matter of fact, the calculated minimum is observed at an intensity of around 6×10^{13} W/cm^2 and the experimental one was found at an energy of 88 μJ, in full agreement with the calibration in Fig. 1.

C. Electron energy calibration

The energy scale of the measured photoelectron spectra is calibrated by means of the energetic distance between neighboring ATI peaks, which corresponds to a photon energy. Note that in our experiment, the zero in kinetic electron energy is unambiguously determined as it corresponds to the center of partially circular patterns in a highly resolved image (see Fig. 2).

III. THEORY

The theoretical results presented in Sec. IV are issued from a complete simulation of the experiment accounting for first, the interaction of Ar with the laser pulse on the atomic scale; second, the macroscopic extension of the interaction
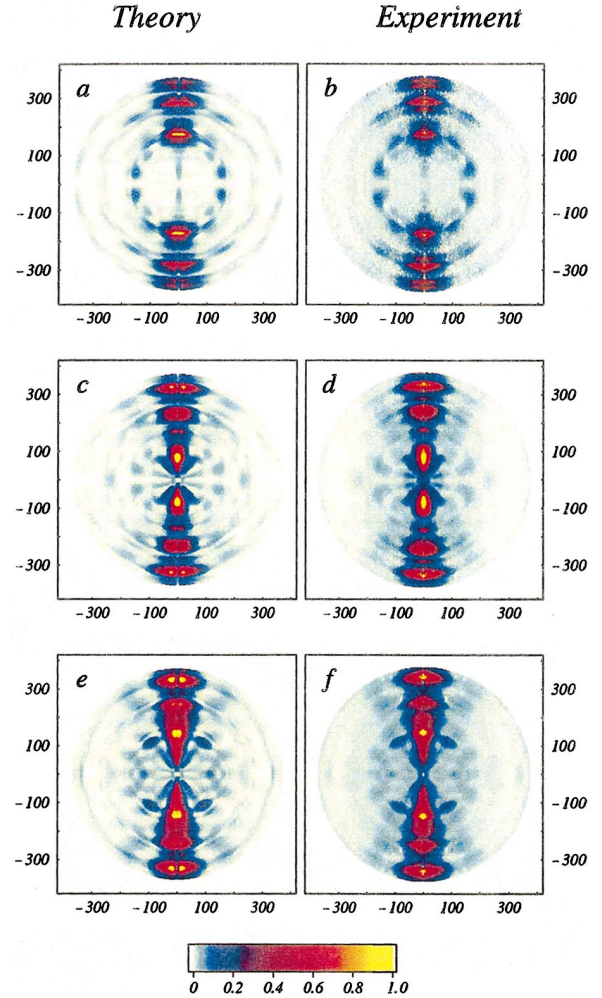
FIG. 2. (Color) Polar plots of the momentum distribution of ATI of Ar for $I = 3.8 \times 10^{13}$ W/cm^2 [(a) and (b)], $I = 5 \times 10^{13}$ W/cm^2 [(c) and (d)], $I = 7 \times 10^{13}$ W/cm^2 [(e) and (f)]. Theory, left; experiment, right.

volume delimited by the laser beam profile; and third, the electron detection procedure as described in Sec. II. The first two parts have been already reported in Ref. [9] and more recently in Ref. [10] and we therefore briefly recall the main lines of the procedure. However, we present in more detail the techniques implemented to simulate the electron detection. Atomic units are used in this section unless otherwise stated.

The first step implies the modelization of the interaction of a single isolated atom and the pulsed electromagnetic field. In other words, it is necessary to determine the final state of the system when the interaction is over. The electrons collected on the detector [see Sec. II] originate from the single ionization of atomic argon (double ionization is orders of magnitude lower for laser peak intensities below 7 $\times 10^{13}$ W/cm^2). The model employed hereafter, therefore, only considers a single active electron (among the 18 that argon possesses) to play a significant role in the interaction, i.e., to be released in the continuum during ionization. The spatiotemporal wave function $\Psi(\mathbf{r}, t)$ corresponding to this active electron is evaluated by numerically solving the asso-

ciated time-dependent Schrödinger equation (TDSE), which reads in our case,

$$i\frac{\partial}{\partial t}\Psi(\mathbf{r},t)=\left[-\frac{1}{2}\nabla^2+V(\mathbf{r})-\mathbf{A}(t)\cdot\mathbf{p}\right]\Psi(\mathbf{r},t). \quad (2)$$

The rather complex attractive atomic potential due to the nucleus screened by the inner-shell electrons is accounted for through the central potential $V(\mathbf{r})=V(r)$. A recently published model potential [11] for argon provides a very accurate description of both the atomic structure (bound states) of the bare atom and the rescattering properties of the ion core. These two features are essential in the present case since ATI is mainly dominated by intermediate resonances due to high-lying Rydberg states for the low-energy photoelectrons and by backscattering on the parent ion core for high-energy photoelectrons.

The interaction with the electromagnetic field is expressed in the velocity gauge and involves the field vector potential related to the electric field by $\mathbf{E}(t)=-(\partial/\partial t)\mathbf{A}(t)$. In the present experiment, the field is linearly polarized and we choose it directed along the z axis. The intensities considered (from around 10^{13} W/cm^2 up to several 10^{14} W/cm^2) as well as the laser wavelength (800 nm) are highly compatible with a semiclassical representation of the field within the dipole approximation. Although the temporal profile of a laser pulse fits, to some extent, a Gaussian envelope, we model it with a cosine square function to get rid of the long Gaussian tails. Thus, the field potential reads

$$\mathbf{A}(t)=\frac{E_0}{\omega}\left(\cos\frac{\pi t}{\tau}\right)^2\sin(\omega t)\mathbf{e}_z, \quad (3)$$

where t varies in $[-\tau/2,\tau/2]$. The peak intensity is therefore given by $I=3.509\times10^{16}E_0^2$ W/cm^2, where E_0 is the maximum field amplitude. τ defines the total pulse duration that leads to an intensity FWHM of $8.806\times10^{-3}\tau$ fs.

The differential Eq. (2) expressed in the spherical set of coordinates is solved numerically by expanding the solution on a radial basis of B splines and an angular basis of spherical harmonics as

$$\Psi(\mathbf{r},t)=\sum_{l=0}^{l_{max}}\sum_{i=1}^{N}c_i^l(t)\frac{B_i(r)}{r}Y_l^0(\theta,\phi). \quad (4)$$

Injecting Eq. (4) in the ordinary differential equation (2) leads to a set of Nl_{max} coupled differential equations that are solved for the unknown coefficients $c_i^l(t)$ using the Crank-Nicholson method. Note that our approach allows to manipulate very large basis sets (up to 100 000 elements in the worst case) since the B-spline discretization method generates extremely sparse matrices.

The electron angular and momentum distribution is computed at the end of the pulse by projecting the total final wave function onto eigenstates corresponding to electrons emitted in the parent ion continuum with a given momentum vector,

$$\frac{\partial P}{\partial E_k\partial\theta_k}=|\langle f_{\mathbf{k}}^-|\Psi(t=\tau/2)\rangle|^2, \quad (5)$$

where $|f_{\mathbf{k}}^-\rangle$ is the Coulomb wave function corresponding to an outgoing electron with momentum $\mathbf{k}$, which reads in terms of partial waves:

$$f_{\mathbf{k}}^-(\mathbf{r})=\sum_{l=0}^{l_{max}}(i)^l e^{-i\delta_l}\Phi_{E_k}^l(\mathbf{r})Y_l^{0*}(\theta_k,0), \quad (6)$$

where δ_l is the Coulombic phase and $\Phi_{E_k}^l(\mathbf{r})$ is a discretized continuum wave function.

The procedure described above provides the probability of observing an electron emitted with a particular energy and direction during ionization of a single atom by the laser field with a given peak intensity. Unfortunately, the experiment collects electrons originating from atoms located anywhere in the interaction volume and therefore experiencing different peak intensities and field phases across the beam profile. This latter fact prevents us from directly comparing the experimental data with the theoretical electron spectra. As a matter of fact, except for low intensity spectra, the ATI peaks never appear at the expected energy location. Moreover, ATI substructures raise or disappear independently in both data. Actually, trying to interpret the measurement on the view of the theoretical results for a single intensity can be misleading. It is therefore a necessity to compute electron spectra resulting from the interaction of the laser beam with all the atoms contained in the interaction volume. This is achieved by computing the yield of electrons emitted in, e.g., the θ_k direction with a kinetic energy E_k as [12]

$$N(E_k,\theta_k)=\rho\int\frac{\partial P(I)}{\partial E_k\partial\theta_k}\frac{\partial V}{\partial I}dI, \quad (7)$$

where ρ is the density of atoms in the chamber (assumed constant). The volume $(\partial V/\partial I)dI$ experiencing an intensity between I and $I+dI$ is defined in Ref. [13] for a Lorentzian (propagation direction) and a Gaussian (transverse direction) beam profile. In practice, less than a hundred partial spectra $\partial P/\partial E_k\partial\theta_k$ corresponding to various intensities are computed. We then interpolate those spectra with respect to I before performing the summation (7).

The multi-intensity photoelectron spectra are used as an input for a simulation of the experiment. Random photoelectron energies and emission angles were generated. The probability was given by the calculated multi-intensity spectra. Experimental parameters are used to calculate the impact position on the detector. The single-electron response of each simulated electron was taken into account by choosing one out of 1000 experimentally determined single event signals. The technique allows us to include the experimental reduction of the resolution due to the limited number of pixels of our CCD device as well as the statistical distribution of the signal produced by one single electron, when it hits the detector. Each theoretical image is the summed signal from
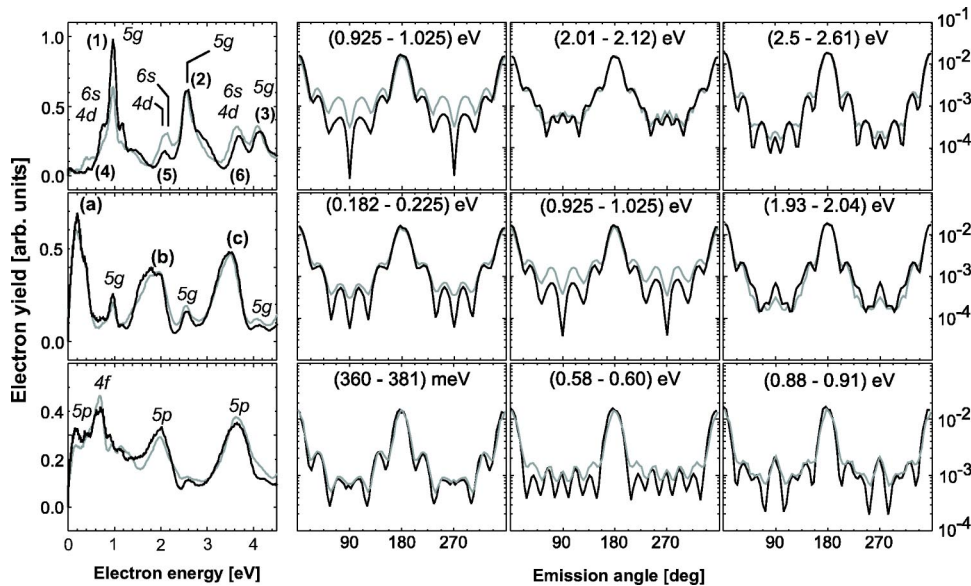
FIG. 3. Electron spectra and angular distribution of several selected ATI peaks of Ar. Top row, $I = 3.8 \times 10^{13}$ W/cm^2; central row, $I = 5 \times 10^{13}$ W/cm^2; and bottom row, $I = 7 \times 10^{13}$ W/cm^2. Note the logarithmic scale on the angular distributions.

10^6 electrons that were subjected to the projection field of the spectrometer in the same way as experimental photoelectrons.

IV. RESULTS AND DISCUSSION

Photoelectron momentum spectra were recorded for intensities varying from $I = 3 \times 10^{13}$ W/cm^2 up to $I = 2 \times 10^{14}$ W/cm^2. Independently, calculations were performed with the same set of parameters. The comparison between experimental and simulated spectra is excellent for the whole range of intensities as discussed below. We have chosen to present a selection of three pairs of images (see Fig. 2), which we consider representative of the various regimes encountered. The radial and angular coordinates in the photoelectron images give the momentum and the ejection angle of photoelectrons. The linear laser polarization is oriented vertical. The probability for detecting an electron is coded into a linear color scale.

A. Channel switching

As can be seen in Fig. 2, drastic changes are observed in the way electrons are ejected from their parent ions as the laser intensity is raised. At low intensity, 11 photons are required to ionize Ar. When the laser strength is increased, the electrons acquire a significant ponderomotive energy (proportional to the field intensity) due to their oscillatory motion in the field. Thus, to achieve ionization, more energy needs to be deposited in the system. Indeed, for intensities above $I = 2 \times 10^{13}$ W/cm^2 12 photons are necessary to bring the system into the continuum. This particular intensity is referred to as the 11-photon ionization channel switching intensity [5]. The successive channels close, in theory, at $I = 4.6 \times 10^{13}$ W/cm^2, $I = 7.2 \times 10^{13}$ W/cm^2, and $I = 9.8 \times 10^{13}$ W/cm^2 for 12-, 13-, and 14-photon ionization, respectively. Shortly after a channel has switched, the ionization is dominated by resonant multiphoton ionization with the high-lying Rydberg states [4,14]. Due to the dipole selection rules,

resonant states have different parity in two successive channels inducing different dynamics. We therefore have chosen to present and discuss spectra corresponding to ionization in the 12-photon ionization channel [(a) and (b) in Fig. 2], at the channel switching [(c) and (d) in Fig. 2], and in the 13-photon ionization channel [(e) and (f) in Fig. 2]. Note that the discussion also holds for higher channel switchings.

A more stringent quantitative comparison is achieved by extracting from the data, energy and angular distributions as shown in Fig. 3. The first column represents the electron energy distribution for the three selected laser peak intensities. These are obtained by integrating over angles from $-10°$ to $10°$. The agreement is very good: both the simulated and measured data exhibit peaks at the same position with comparable amplitudes for all intensities. The channel switching is well illustrated by comparing spectra (a), (b) and (e), (f). Clearly, the resonances involved in each process are different. To get a better insight, we have plotted the angular distribution corresponding to the labeled selected peaks (the three columns on the right). The angular distributions reveal the parity and the dominant angular-angular momentum of the emitted electrons at that particular energy.

B. Resonant ionization

The accurate simulation allows to recover the full dynamics and a reliable identification of the resonances as demonstrated below. Although we illustrate the discussion in a single particular case, all spectrum peaks have been investigated through the same procedure.

Multiphoton ionization and, consequently, above-threshold ionization requires high field intensities according to the high nonlinearity of the process. A minimum of 12 photons need to be absorbed to bring the system into the first continuum. Ionization is therefore expected to vary as I^{12}. Any of these high-order processes should, in principle, produce a significant contribution when the field is at the peak intensity. In the experiment, however, the situation is different because the incident laser beam has a spatial dependence.
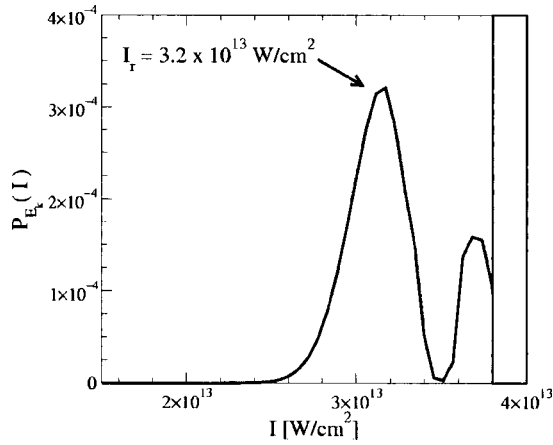
FIG. 4. Intensity dependence of the electron yield with E_k $=1$ eV for a peak intensity of $I=3.8\times10^{13}$ W/cm^2. The main contribution is from atoms experiencing a resonant intensity of I_r $=3.2\times10^{13}$ W/cm^2.

Apart from ionizing the system, the field also induces a distortion and ac Stark shifts the atomic levels. Accordingly, the ionization potential is increased by the ponderomotive energy U_p. This modification of the atomic structure dynamically induces resonances that boost the ionization when the detuning vanishes (REMPI). Note that the resonance can take place before or after the laser pulse maximum. For a given peak intensity, an electron detected with a particular kinetic energy may have been emitted long before the field maximum. Alternatively, this electron may come from a location in the interaction volume which is off the propagation axis and therefore originating from an atom experiencing a lower temporal peak intensity.

These contributions might dominate the spectrum since the ionization enhancement due to a particular resonance (which happens for an atom experiencing a fixed intensity) always produces electrons at the same energy. No matter where or when they have been emitted, the contributions add up at the same energy in the spectrum, thus giving peaked structures.

Let us consider the peak labeled (1) in the upper left graph in Fig. 3. The experiment informs us that the electrons contributing to that peak are emitted with a kinetic energy of $E_{(1)}=0.0363$ a.u. (0.99 eV) and an angular momentum dominated by $l=5$ (five minima in the angular distribution). In order to get a better insight of the process, we first have considered the production of electrons (from a single atom) with kinetic energy $E_{(1)}$ as a function of the maximum temporal field intensity. The production of such electrons has a sharp peak centered around an intensity of $I_{(1)}=3.2$ $\times10^{13}$ W/cm^2 (the maximum intensity being in that case $I_{(1)}=3.8\times10^{13}$ W/cm^2) as shown in Fig. 4). The detected electrons at $E_{(1)}$ are thus originating from those locations where, due to the spatial beam distribution, the local temporal field maximum intensity is $I_{(1)}=3.2\times10^{13}$ W/cm^2. By checking the population created at $E_{(1)}$ with a field intensity $I_{(1)}$ we have found the following angular momentum distribution: 66.5% in $l=5$, 17.5% in $l=7$, 9% in $l=1$, and 7% in $l=3$. The domination of $l=5$ is in agreement with the

measured angular distribution. At this rather low intensity, a resonant process is restricted to 11-photon resonant 12-photon ionization. According to the dipole selection rules and the fact that $l=5$ clearly dominates, this resonant state belongs either to the $l=4$ or $l=6$ symmetry. If we now assume that the high-lying Rydberg states ponderomotively shift as the ionization potential (i.e., by U_p), the resonant level should lie around $E=-0.020\,65$ a.u. The nearest candidate is the $5g$ state ($E_{5g}=-0.02$ a.u.) which, in theory, shifts into resonance with the absorption of 11 photons at an intensity of $I=2.9\times10^{13}$ W/cm^2. The discrepancy observed between these two intensities might be due to two reasons. On the one hand, we have made the assumption that the state shifts upward like the ionization threshold. It might happen that the energy shift is affected by a quasiresonant one- or two-photon coupling to another bound state, thus modifying the resonant intensity. We have observed that this argument is valid only for low-lying Rydberg states. On the other hand, the resonant process should last for a while for the production of electrons to be significant. Therefore, we expect that the observed resonance intensity is higher than the theoretical one, so that resonant ionization lasts several femtoseconds around the field peak intensity. This identification is reenforced by looking at the bound states dynamics during the interaction. In Fig. 5 we compare the time-dependent populations of two types of Rydberg states, namely, the g series and the $5d$. They both dynamically shift into resonance. However, the g series is responsible for a great enhancement and, in particular, the $5g$ state, while the $5d$ is not. The behavior is very different: the contributing states keep a significant population at the end of the pulse (spontaneous deexcitation is not accounted for in the model), while the other does not.

The remaining 17.5% of the population in $l=7$ is still due to the $5g$ resonance, which is coupled to the $l=7$ continuum through three photons (most probably two photons absorbed and one emitted). This scheme is confirmed by the dominance of $l=6$ in the first ATI peak labeled (3) [see the angular distribution in Fig. 3].

As a matter of fact, peaks (1), (2), and (3), separated by an exact photon energy, all originate from atoms that went through resonance with the $5g$. Similarly, peaks (4), (5), and (6) are populated by electrons emitted from other locations and other times and due to another resonant state. Applying the same procedure, we have found that the contribution comes from the $4d$ (going through resonance at $I=3.64$ $\times10^{13}$ W/cm^2) and the $6s$ (going through resonance at I $=3.55\times10^{13}$ W/cm^2). These resonances are close to each other and are not resolved by the experiment (but are distinguishable in the high-resolution calculations) leading to the production of a broad peak [see peaks (5) and (6)]. As expected, the leading angular momenta observed are $l=5$, l $=6$, and $l=7$ for the peaks (1), (2), and (3), respectively, and $l=3$, $l=4$, and $l=5$ for the peaks (4), (5), and (6). Note that the angular distribution of peak (5) reveals eight minima. In all cases, the peaks contain a mixture of angular momenta [even symmetry for peak (5)]. The number of minima in the angular distribution is determined by the highest l value, which is 8 in that case. However, a close look to
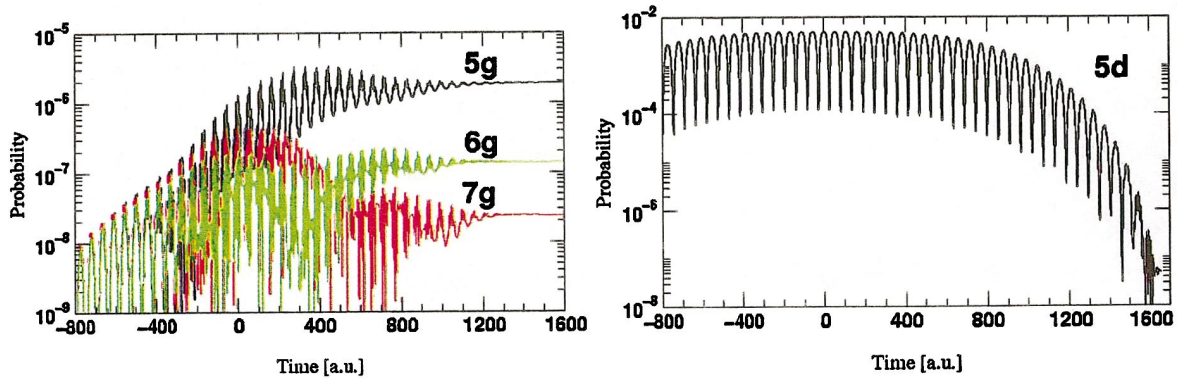
FIG. 5. (Color) Populations of the $5d$ and few g states as a function of time. Note the particular behavior of the g states (keeping population at the end of the pulse), which play a significant enhancing role in ionization compared to the inoperative $5d$. $I=3.8 \times 10^{13}$ W/cm^2.

the simulated data shows, at the energy of peak (5), a dominance of $l=4$. The experimental resolution is sufficient to resolve the substructure located on the right side of peak (1) due to the $6g$. The higher resonances ($7g$, $8g$, ...) are not resolved but generate the broad pedestal between 1.2 and 1.8 eV.

The second row of graphs from Fig. 3, measured for an intensity of $I=5\times10^{13}$ W/cm^2, is an intermediate situation where the ionization potential has shifted in such a way that 12-photon resonant 13-photon ionization is now possible: channel switching happens at $I=4.6\times10^{13}$ W/cm^2. Because different parity states come into resonance, a new comb of peaks arises while the other comb tends to disappear. These new peaks, labeled (a), (b), and (c), seem, at the first glance, to be due to a resonance with the $4d$ state (at $I=3.7 \times 10^{13}$ W/cm^2). This is consistent with the angular distribution of peak (b). However, a deeper look reveals a more complicated situation, which we discuss in the following section.

Finally, the last row in Fig. 3, corresponding to an intensity of $I=7\times10^{13}$ W/cm^2, reveals a regime in between two successive channel closures. The dominant comb of peaks seen for the low intensity case has completely disappeared and the spectrum is now dominated by the comb due to the $5p$ and the $4f$ resonances with 12 photons. The peaks are more or less centered on the $5p$ resonance which occurs at $I=6.35\times10^{13}$ W/cm^2 (confirmed by their respective angular distributions of $l=5$ and $l=6$). The broadening is due, on the high-energy side, to the embedded resonance with the $4f$ state (which is well resolved in the first ATI peak) and, on the low-energy side, to nonresonant ionization.

C. ac Stark splitting

By omitting the detection process in the simulation, a higher resolution is achieved and the computation clearly shows that peak (b) in Fig. 3, in fact, contains two sharp resonances (at energies of 1.81 eV and 2 eV) and a broad structure centered at 1.6 eV as can be seen in Fig. 6. The broad structure, unlike Freeman resonances, shifts downward as the intensity is increased, characterizing a nonresonant ATI process (see the following section). The higher reso-

nance (at 2 eV) is safely attributed to $(11+2)$-photon ATI through $4d$. However, there is no state to trivially assign to the lower resonance. The energy levels of argon are such that the $4d$ is almost resonantly coupled with the inner $4p$ state by a photon of 1.55 eV. Since the applied field is very strong, the coupling will repel these two states and lead to a splitting of the ionization peak. The structure at 1.81 eV is therefore due to the $4p$ and the double structure results from the dressed transition $4p$-$4d$. The evidence for that is, unlike isolated Rydberg resonances, the peak attributed to $4p$ shifts downward as the intensity is increased, giving rise to the ac-Stark splitting.

D. Nonresonant ionization

The broadening observed in the peak around 1.8 eV in Fig. 6 is not only due to the splitting but also to nonresonant ionization. Unlike resonant ionization where the contributions always add up at the same electron energy, nonresonant
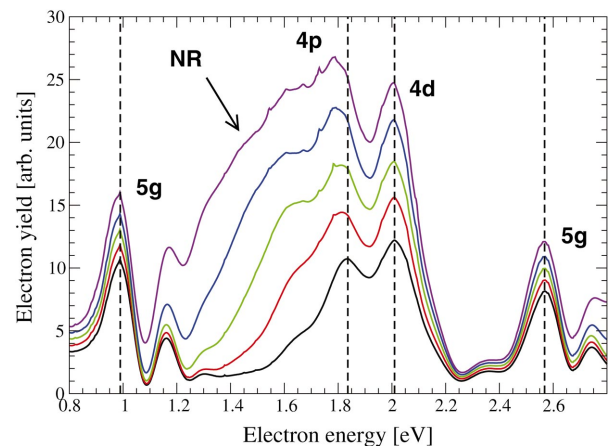
FIG. 6. (Color) High-resolution simulated electron distribution at $\theta=0°$ as a function of intensity. The central peak corresponds to peak (b) in Fig. 3. The intensities range from $I=4.6\times10^{13}$ W/cm^2 to $I=5.4\times10^{13}$ W/cm^2. Note the nonresonant ionization located between 1.3 and 1.7 eV that shifts downward with increasing intensity. Note also the double structure splitting for higher field strength.

peaks shift downward by the ponderomotive energy U_p as the intensity is raised. Note also that the peak amplitude increases more rapidly. This situation happens over intensity ranges where no Rydberg states come into resonance [15]. We have observed it only in the high-resolution spectra of Ar, but it happens to be more visible in ATI of Xe [3]. The measurement shows that peak (a) in Fig. 3 is dominated by $l=5$ instead of $l=3$ for the resonant process. This feature is the signature that the split structure originating from the $4p$-$4d$ dressed transition is embedded in the nonresonant background.

V. CONCLUSION

The dynamics of ATI of argon has been investigated through both experimental and theoretical approaches. The experimental momentum distributions have been successfully reproduced in great detail through a complete theoretical calculation of the experiment including: (1) the single atom response (nonperturbative theory), (2) the integration over the interaction volume, and (3) the simulation of the detection procedure. The merging of the information coming from both the experimental and the calculations allows a robust identification of the many processes involved (channel switching, resonant ionization, . . .) in the ATI of Ar. The availability of a higher resolution in the theoretical data has revealed nonresonant ionization as well as ac Stark splitting.

[1] G.G. Paulus, W. Nicklich, H. Xu, P. Lambropoulos, and H. Walther, Phys. Rev. Lett. **72**, 2851 (1994).

[2] L. F. DiMauro and P. Agostini, *Advances in Atomic-Molecular and Optical Physics* (Academic, New York, 1995), Vol. 35.

[3] R. Wiehle and B. Witzel, Phys. Rev. Lett. **89**, 223002 (2002).

[4] R.R. Freeman, P. Bucksbaum, H. Milchberg, S. Darack, D. Scumacher, and M.E. Geusic, Phys. Rev. Lett. **59**, 1092 (1987).

[5] V. Schyja, T. Lang, and H. Helm, Phys. Rev. A **57**, 3692 (1998).

[6] H. Helm, N. Bjerre, M.J. Dyer, D.L. Huestis, and M. Saeed, Phys. Rev. Lett. **70**, 3221 (1993).

[7] C. Bordas, F. Pauling, H. Helm, and D.L. Huestis, Rev. Sci. Instrum. **67**, 2257 (1996).

[8] E. Cormier, D. Garzella, P. Breger, P. Agostini, G. Chriaux, and C. Leblanc, J. Phys. B **34**, L9 (2001).

[9] E. Cormier and P. Lambropoulos, J. Phys. B **30**, 77 (1997).

[10] H. Bachau, E. Cormier, P. Decleva, J.E. Hansen, and F. Martín, Rep. Prog. Phys. **64**, 1815 (2001).

[11] H.G. Muller and F.C. Kooiman, Phys. Rev. Lett. **81**, 1207 (1998).

[12] M.A. Walker, P. Hansch, and L.D.V. Woerkom, Phys. Rev. A **57**, R701 (1998).

[13] S. Augst, D.D. Meyerhofer, D. Strickland, and S.L. Chin, J. Opt. Soc. Am. B **8**, 858 (1991).

[14] P. Agostini, P. Breger, A. L'huillier, H.G. Mueller, and G. Petite, Phys. Rev. Lett. **63**, 2208 (1989).

[15] H. Helm and M.J. Dyer, Phys. Rev. A **49**, 2726 (1994).